Astronomy & Astrophysics

Kepler-93: A testbed for detailed seismic modelling and orbital evolution of super-Earths around solar-like stars

J. Bétrisey[1] , C. Pezzotti[1], G. Buldgen[1], S. Khan[2,3], P. Eggenberger[1], S. J. A. J. Salmon[1], and A. Miglio[4,5]

[1] Observatoire de Genève, Université de Genève, Chemin Pegasi 51, 1290 Versoix, Switzerland
e-mail: Jerome.Betrisey@unige.ch
[2] Institute of Physics, Laboratory of Astrophysics, École Polytechnique Fédérale de Lausanne (EPFL), Observatoire de Genève, Chemin Pegasi 51, 1290 Versoix, Switzerland
[3] School of Physics and Astronomy, University of Birmingham, Edgbaston, Birmingham B15 2TT, UK
[4] Dipartimento di Fisica e Astronomia, Università degli Studi di Bologna, Via Gobetti 93/2, 40129 Bologna, Italy
[5] INAF – Astrophysics and Space Science Observatory Bologna, Via Gobetti 93/3, 40129 Bologna, Italy

ABSTRACT

Context. The advent of space-based photometry missions such as CoRoT, *Kepler* and TESS has sparkled the rapid development of asteroseismology and its synergies with exoplanetology. In the near future, the advent of PLATO will further strengthen such multi-disciplinary studies. In that respect, testing asteroseismic modelling strategies and their importance for our understanding of planetary systems is crucial.
Aims. We carried out a detailed modelling of Kepler-93, an exoplanet host star observed by the *Kepler* satellite for which high-quality seismic data are available. This star is particularly interesting because it is a solar-like star very similar to the PLATO benchmark target (G spectral type, $\sim$6000 K, $\sim$1 $M_\odot$ and $\sim$1 $R_\odot$) and provides a real-life testbed for potential procedures to be used in the PLATO mission.
Methods. We used global and local minimisation techniques to carry out the seismic modelling of Kepler-93, for which we varied the physical ingredients of the given theoretical stellar models. We supplemented this step by seismic inversion techniques of the mean density. We then used these revised stellar parameters to provide new planetary parameters and to simulate the orbital evolution of the system under the effects of tides and atmospheric evaporation.
Results. We provide the following fundamental parameters for Kepler-93: $\bar{\rho}_\star = 1.654 \pm 0.004$ g cm^{-3}, $M_\star = 0.907 \pm 0.023\,M_\odot$, $R_\star = 0.918 \pm 0.008\,R_\odot$, and Age $= 6.78 \pm 0.32$ Gyr. The uncertainties we report for this benchmark star are well within the requirements of the PLATO mission and give confidence in the ability of providing precise and accurate stellar parameters for solar-like exoplanet-host stars. For the exoplanet Kepler-93b, we find $M_p = 4.01 \pm 0.67\,M_\oplus$, $R_p = 1.478 \pm 0.014\,R_\oplus$, and a semi-major axis $a = 0.0533 \pm 0.0005$ AU. According to our simulations of the orbital evolution of the system, it seems unlikely that Kepler-93b formed with a mass high enough ($M_{\rm p,initial} > 100\,M_\oplus$) to be impacted on its orbit by stellar tides.
Conclusions. For the benchmark case of a solar twin of the PLATO mission, detailed asteroseismic modelling procedures will be able to provide fundamental stellar parameters within the requirements of the PLATO mission. We also illustrate the synergies that can be achieved regarding the orbital evolution and atmospheric evaporation of exoplanets when these parameters are obtained. We also note the importance of the high-quality radial velocity follow-up, which here is a limiting factor, for providing precise planetary masses and mean densities to constrain the formation scenarii of exoplanets.

Key words. planetary systems – stars: fundamental parameters – asteroseismology – planet-star interactions – stars: individual: Kepler-93

1. Introduction

In the past decade, astonishing progresses were achieved in asteroseismology through the revolution initiated by the high-quality data from the space-based missions CoRoT (Baglin et al. 2009), *Kepler* (Borucki et al. 2010), and TESS (Ricker et al. 2015). With the future mission PLATO (Rauer et al. 2014), the field will again experience a breakthrough as it will observe bright stars in the southern hemisphere with an expected precision comparable to *Kepler* and will benefit by a better radial velocity (RV) follow-up than in the northern hemisphere. Aster-oseismic measurements allow a precise characterisation of stellar parameters, such as mass, radius, and age, which can hardly be reached with other standard techniques for non-binary stars. Complementary to the benefits for asteroseismology, these missions contributed significantly to the development of exoplanet

detections (Bordé et al. 2003; Borucki et al. 2010; Sullivan et al. 2015; Barclay et al. 2018; Rauer & Heras 2018). In this context, we exploited the asteroseismic data of the *Kepler* Space Telescope, whose capabilities for exoplanetology and asteroseismology allow great synergies between these fields. The exoplanet detection itself does not rely on approaches that depend on stellar models, and thus, a detailed characterisation of the host star significantly improves the understanding of the exoplanet(s) (see e.g. Christensen-Dalsgaard et al. 2010; Huber et al. 2013; Campante et al. 2018).

We chose to focus on Kepler-93, which is known as KOI 69 or KIC 3544595 in the literature. This host star possesses high-quality asteroseismic data (Davies et al. 2016). In addition, it presents $\log(g) = 4.52 \pm 0.20$ dex, [Fe/H] $= -0.18 \pm 0.10$ dex, $T_{\rm eff} = 5718 \pm 100$ K (Furlan et al. 2018), and $m_V = 10.00 \pm 0.03$ (Høg et al. 2000), making it a benchmark target for PLATO

because the data quality is similar to the expectations for this mission and motivating a new characterisation to reach the precision requirements (2% for the radius, 15% for the mass, and 10% for the age). Its stellar parameters were first determined using scaling relations by Huber et al. (2013). Marcy et al. (2014) performed a similar analysis and reported comparable results. A more detailed modelling of the star, considering the information contained in the individual frequencies, was performed by Ballard et al. (2014), who were able to provide better-constrained parameters. A new analysis using BASTA was conducted by Silva Aguirre et al. (2015). They estimated the impact of the change in some physical ingredients based on their sample of 33 targets and found stellar parameters with a precision (random and systematic) comparable to Ballard et al. (2014), which used a grid of evolutionary models with a fixed Y/Z ratio. Finally, new analyses were performed using a machine-learning algorithm (Bellinger et al. 2016, 2019). Their precision is comparable to the previous works, which used a single grid with fixed physical ingredients, and therefore did not investigate the systematics caused by their variations.

The star Kepler-93 is known to host at least two exoplanets. The high photometric precision of the Kepler-93 observations enabled a detection of an exoplanet, Kepler-93b, during the first four months of *Kepler* data (Borucki et al. 2011). Marcy et al. (2014) provided a first estimation of the planetary mass ($2.6 \pm 2.0\,M_\oplus$) on the base of 32 Keck HIRES RV observations from July 2009 to September 2012. They also detected the presence of a perturbing companion (Kepler-93c), for which they calculated lower limits on the mass ($M > 3\,M_{\rm Jup}$) and orbital period ($P > 5\,{\rm yr}$). Ballard et al. (2014) derived a very precise best-fit value for the radius measurements of Kepler-93b, which is $1.481 \pm 0.019\,R_\oplus$, from which they estimated an average planetary density of $6.3 \pm 2.6\,{\rm g\,cm^{-3}}$, which is compatible with the density of a rocky world. On the base of 86 RV observations obtained with the HARPS-N spectrograph on the Telescopio Nazionale *Galileo* and 32 archival Keck/HIRES observations, Dressing et al. (2015) provided a more precise mass estimate of Kepler-93b ($4.02 \pm 0.68\,M_\oplus$) and derived a relatively higher density of $6.88 \pm 1.18\,{\rm g\,cm^{-3}}$, which is consistent with a rocky composition primarily of iron and magnesium. The precise determination of the radius and density of Kepler-93b, indicating a rocky-world composition with almost no volatile elements, together with the availability of high-quality asteroseismic data of the host star, enable us to perform a study that relates the rotational history of Kepler-93 with the evolution of the planet for the first time. Because Kepler-93b probably lost its atmosphere during the early stages of the evolution, we aim to test the impact of the X-ray and extreme ultraviolet (XUV) fluxes received by the planet that account for its eventual migration due to the dissipation of tides in the stellar convective envelope, considering different rotational histories of the host star. Specifically, we wish to test whether if it were a very slow rotator, Kepler-93b could retain a fraction of its primordial atmosphere at its current age. With this type of study, we aim to understand the mechanisms that concur in shaping the radius valley (see e.g. Van Eylen et al. 2018), accounting for a dedicated computation of the high-energy irradiation emitted by the host star throughout its evolution, together with the impact of tides.

In this paper, we provide a detailed modelling of Kepler-93 and then characterise the evolution of Kepler-93b. In Sect. 2 we carry out a two-step forward modelling, consisting of a global minimisation to restrict the parameter space, followed by a local minimisation where we consider extensive changes in the physical ingredients. We also compare between the direct fit of the

individual frequencies and a more refined method, the fit of frequency ratios, to illustrate the relevance of fitting the frequency ratios instead of the individual frequencies. In Sect. 3 we conduct inversions to provide a more robust estimation of the mean density and test different prescriptions for the surface effects. Based on the improvement of the precision on the stellar parameters, we revise the planetary parameters of Kepler-93b. In Sect. 4 we study the evolution of Kepler-93b under the impact of stellar tides and evaporation of the planetary atmosphere by coupling the optimal stellar model of Kepler-93 to our orbital evolution code. Finally, in Sect. 5 we draw the conclusions of our study of the Kepler-93 system.

2. Forward modelling

The oscillation modes of Kepler-93 were estimated using the so-called peak bagging by Davies et al. (2016). This technique relies on a Bayesian approach and on a standard Metropolis-Hastings Monte Carlo Markov chain (MCMC, see e.g. Gelman et al. 2013 for an introduction to MCMC techniques). The output quality was assessed with an unsupervised machine-learning Bayesian scheme. Complementary to the asteroseismic data, we searched in the literature for spectroscopic measurements that provide good and independent constraints on the stellar metallicity, the effective temperature and the surface gravity. We adopted the values of Furlan et al. (2018) with their recommended error: $\log(g) = 4.52 \pm 0.20$ dex, $[{\rm Fe/H}] = -0.18 \pm 0.10$ dex and $T_{\rm eff} = 5718 \pm 100$ K. They provide a reanalysis of the KOI targets with several algorithms, which allowed them to quantify the systematic error associated with the deviations observed between the different routines used to derive the spectroscopic parameters. These data were part of a survey, which explains the conservative precision on the estimated values.

The luminosity was computed using the following formula:

$$\log\left(\frac{L}{L_\odot}\right) = -0.4\left(m_\lambda + {\rm BC}_\lambda - 5\log d + 5 - A_\lambda - M_{\rm bol,\odot}\right), \quad (1)$$

where m_λ, ${\rm BC}_\lambda$, and A_λ are the magnitude, the bolometric correction, and the extinction in a given band λ. We used the 2MASS K_s-band magnitude properties. The bolometric correction was estimated using the code written by Casagrande & VandenBerg (2014, 2018), and the extinction was inferred with the Green et al. (2018) dust map. A value of $M_{\rm bol,\odot} = 4.75$ was adopted for the solar bolometric magnitude. Two different methods have been tested to obtain the distance d in pc from *Gaia* (Gaia Collaboration 2018): either directly inverting the parallax or using the published distance from Bailer-Jones et al. (2018). Both lead to similar luminosity estimates, $L = 0.82 \pm 0.03\,L_\odot$, which is the value adopted in this paper.

All the stellar evolutionary sequences in this work were computed with the Code Liégeois d'Évolution Stellaire (CLES; Scuflaire et al. 2008a) and the adiabatic frequencies and eigenfunctions with the Liège Oscillation Code (LOSC; Scuflaire et al. 2008b). The modelling is articulated in two steps. In a first step, a global minimisation was conducted to restrict the parameter space. Here, we used the AIMS software (Rendle et al. 2019), which is an MCMC-based algorithm. Then, the impact of the physical ingredients was investigated. For this purpose, we used a local minimisation method, the Levenberg-Marquardt algorithm (see e.g. Roweis 1996). The MCMC algorithm runs with four free parameters, the mass M, the age τ, and

the initial chemical composition, in which X_0 is the initial hydrogen mass fraction and Z_0 is the heavy elements mass fraction. For the Levenberg-Marquardt algorithm, we included one additional free parameter, the mixing-length parameter α_{MLT}. This technique is indeed much faster and allows a more detailed exploration of the parameter space, but only at a local level. If surface effects were considered, they were described by two additional free parameters.

2.1. Global minimisation

For the global minimisation, a grid of models was first generated by varying the mass ($M_{\min} = 0.70\,M_\odot$, $M_{\max} = 1.10\,M_\odot$, $M_{\mathrm{step}} = 0.02\,M_\odot$), the initial hydrogen mass fraction ($X_{0,\min} = 0.72$, $X_{0,\max} = 0.77$, $X_{0,\mathrm{step}} = 0.01$), and the initial heavy elements mass fraction ($Z_{0,\min} = 0.006$, $Z_{0,\max} = 0.013$, $Z_{0,\mathrm{step}} = 0.001$) and keeping the following physical ingredients fixed. We used the AGSS09 abundances (Asplund et al. 2009) and the OPAL opacities (Iglesias & Rogers 1996), supplemented by the Ferguson et al. (2005) opacities at low temperature and the electron conductivity by Potekhin et al. (1999) and Cassisi et al. (2007). The FreeEOS equation of state (Irwin 2012) was used, and the microscopic diffusion was described by the formalism of Thoul et al. (1994), but with the screening coefficients of Paquette et al. (1986). Convection is implemented using the mixing-length theory (MLT) as in Cox & Giuli (1968), and the nuclear reaction rates were taken from Adelberger et al. (2011). The mixing-length parameter α_{MLT} is fixed at a solar calibrated value. Finally, for the atmosphere modelling, we used the $T(\tau)$ relation described by Model-C in Vernazza et al. (1981, hereafter VAL-C).

The minimisation was performed with the AIMS software (Rendle et al. 2019), which is based on an MCMC algorithm (EMCEE, Foreman-Mackey et al. 2013) and a Bayesian statistics approach to provide the probability distributions for the stellar parameters. The MCMC uses an interpolation scheme to sample between the grid points. This interpolation reduces the fineness of the grid required to have a sufficient sampling of the parameter space. This approach is well suited for main-sequence stars whose solution is not too degenerate. We remark that in our case, the combination of small steps for the grid and the interpolation within these steps resulted in a very fine exploration of the parameter space. All the priors of the free variables are uninformative, except for the age prior, which is the uniform distribution on the interval [0,14] Gyr. We used Gaussian priors for the constraints. In addition to the classical constraints (in our case, the effective temperature, luminosity, and metallicity), we considered two sets of seismic constraints in AIMS: the observed individual frequencies, and the frequency ratios. We used the r_{01} and r_{02} ratios, according to the definitions of Roxburgh & Vorontsov (2003). It is possible to replace the r_{01} ratios by the r_{10}, but because they are not independent, they should not be used together, because that will introduce a bias (Roxburgh 2018). In general, the fit of the ratios requires an estimate of the mean density as additional constraint because the information about the mean density is suppressed from the ratios in their definition, as they are normalised by the large frequency separation that is a proxy of the mean density (Vandakurov 1967). We therefore carried out a mean density inversion (see Sect. 3 for a detailed explanation of what a mean density inversion is) on the model resulting from the fit of the frequencies. Because this inverted mean density is the result of the inversion of only one model, we considered a conservative error. The final mean density quoted in Table 3 is the result of a more elaborated

Table 1. Main stellar parameters predicted by AIMS for the models based on the fit of the frequencies and on the fit of the r_{01} and r_{02} ratios.

Seismic constraints	ν_{nl}	r_{01} and r_{02}
$M/M_\odot$	0.923 ± 0.024	0.907 ± 0.017
$R/R_\odot$	0.923 ± 0.017	0.918 ± 0.006
τ (Myr)	6786 ± 259	6780 ± 235
$\bar{\rho}$ (g cm^{-3})	1.655 ± 0.057	1.653 ± 0.010
X_0	0.753 ± 0.014	0.744 ± 0.014
Y_0	0.237 ± 0.014	0.247 ± 0.014
Z_0	$(9.8 \pm 1.3) \times 10^{-3}$	$(9.1 \pm 1.2) \times 10^{-3}$

Notes. The errors are statistical errors.

procedure that is also described in Sect. 3. Hence, we adopted a mean density estimate of $1.654 \pm 0.010\,\mathrm{g\,cm^{-3}}$. This guess is consistent with the final mean density provided in this work.

The first MCMC minimisation was conducted with the individual frequencies as constraints and the two-term surface effect correction from Ball & Gizon (2014) (cf. Eqs. (5) and (6)). The best MCMC model was coherent, because it reproduced the observed échelle diagram. However, the mode identification of AIMS revealed a shift with respect to the identification of Davies et al. (2016). Appendix B shows that the asymptotic behaviour of the ϵ_{nl} phases (White et al. 2012; Roxburgh 2016) with the identification of Davies et al. (2016) is inconsistent, because they lie significantly below 1, which is unexpected. The corrected identification can be found in Appendix A. After the mean density inversion on the model resulting from the fit of the frequencies, we performed a second MCMC minimisation in which we added the inverted mean density to the constraints and replaced the individual frequencies by the frequency ratios. The fit of the ratios was made without surface effects. The ratios are indeed designed to reduce the impact of surface effects (Roxburgh & Vorontsov 2003), and it is thus difficult to estimate them with this set of constraints. The corner plot of the MCMC fitting the frequency ratios can be found in Appendix C. This plot shows the distributions and correlations of the stellar mass, helium content, metallicity, age (which are the optimized parameters), and radius. The addition of the inverted mean density to the constraints especially improves the precision in determining mass and radius. The mean density of the forward modelling is strongly constrained by the assumption about the value and uncertainty on the inverted mean density, which is not an issue because the mean density inversion is quasi-model-independent and we also assumed a conservative uncertainty to avoid biases. For Kepler-93, we found that the r_{01} ratios improve the precision for the age, but the mean density does not. The central hydrogen value X_{c} (and hence the age) is already well constrained by the seismic information in the case of Kepler-93. For stars with a less well constrained X_{c}, it would be interesting to study whether the gain in mass precision through the mean density might help to constrain the age better.

The main stellar parameters for the two sets of constraints are displayed in Table 1. A comparison between the histograms of both sets is shown in Fig. 1. On one hand, the fit of the frequencies is more sensitive to the grid. Small peaks can be seen at the top of the histograms, which indicate that the walkers tend to become stuck on the grid points during the exploration of the parameter space. This effect is not observed for the fit of the ratios and their smooth histograms. On the other hand, the fit of the frequencies tends to overestimate the stellar mass. This
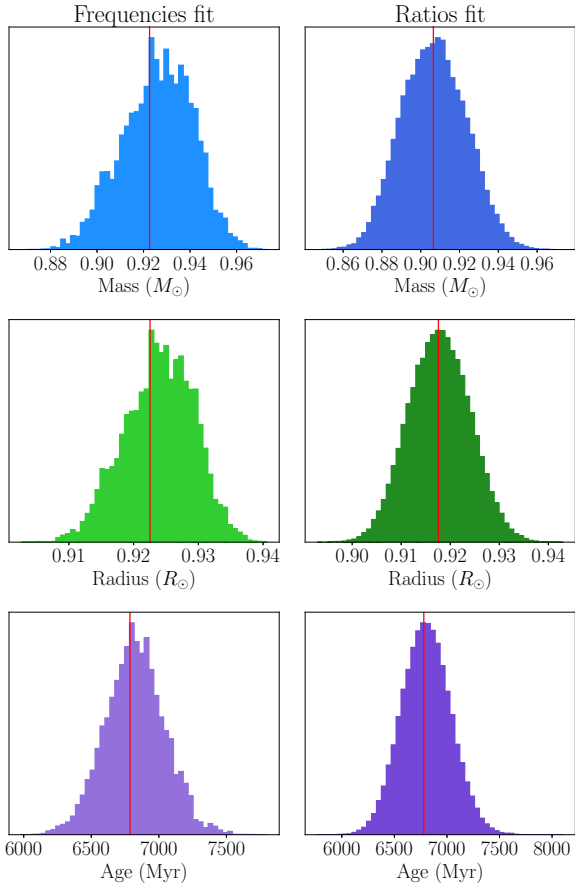
Fig. 1. Comparison of the histograms between the fit of the individual frequencies (*left column*) and of the frequency ratios r_{01} and r_{02} (*right column*). *Upper panel*: histogram for the stellar mass. *Middle panel*: histogram for the stellar radius. *Lower panel*: histogram for the stellar age. The vertical red lines indicate the optimal estimates predicted by the MCMC.

trend is linked with the treatment of the surface effects, which is empirical and thus not optimal. This overestimation is problematic because Rendle et al. (2019) found that their software produces very peaked distributions when fitting the frequencies, which can lead to a precise but biased mass value. A similar behaviour was also observed by Miglio & Montalbán (2005), Buldgen et al. (2019a), and Salmon et al. (2021).

In Fig. 2 we show the échelle diagram of the results from the fit of the two sets of seismic constraints. They both agree with the observed frequencies. The ratios r_{01}, r_{10}, and r_{02}, displayed in Fig. 3 are also well reproduced. The bump at high frequencies for r_{01} and r_{10} is likely due to surface activity. A shift in the frequencies due to surface activity was observed for the Sun by Howe et al. (2018, 2020) or in the *Kepler* data by Santos et al. (2018). Concerning the ratios, Thomas et al. (2021) observed that surface activity has an impact on the r_{02} ratios, especially at high frequencies. No investigation has been conducted on r_{01} and r_{10} to date, but based on the literature and because the bump is at high frequencies, it is very possible that this is the case.

The initial helium mass fraction Y_0 of the model fitting the frequencies is slightly lower than the value of the primordial helium mass fraction $Y_p \simeq 0.247$ (Pitrou et al. 2018). Even though Kepler-93 is a metal-poor star, we do not expect a helium mass fraction close to the primordial value. However, the precision on the frequencies is insufficient to make use of glitch-fitting techniques to directly constrain the helium abundance in
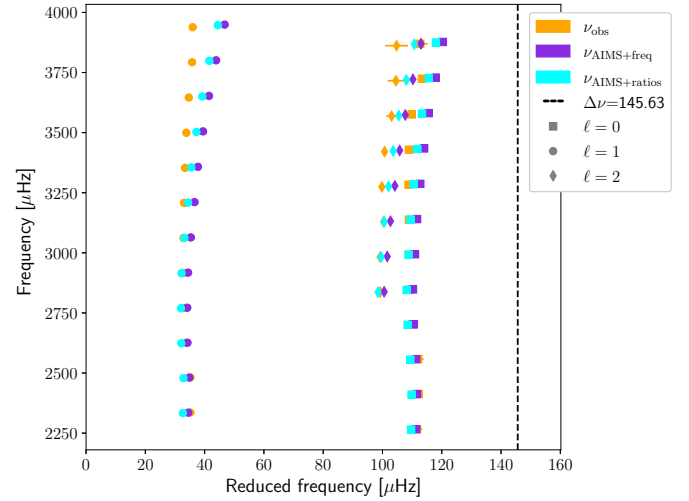
Fig. 2. Echelle diagram of the AIMS results for the fit of the individual frequencies (purple) and of the frequency ratios r_{01} and r_{02} (cyan). The modelled frequencies are displayed without a correction for the surface effects. The large separation (dashed black line) is computed with the observed frequencies (orange) and with the definition of Reese et al. (2012). The squares are radial modes, the circles are dipole modes, and the diamonds are quadrupole modes.
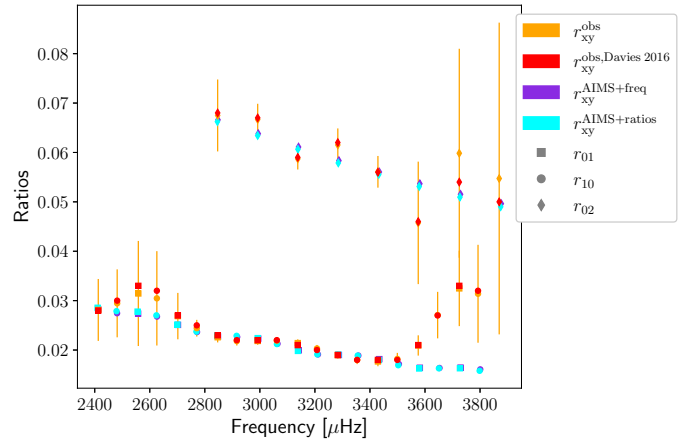
Fig. 3. Observed and modelled frequency ratios r_{01}, r_{10}, and r_{02} of Kepler-93. In red we plot the ratios computed by Davies et al. (2016) without error bars for readability reasons. These errors are similar to those found in this work. The observed ratios of our study (orange) are computed with the definitions of Roxburgh & Vorontsov (2003), while the ratios from Davies et al. (2016) come from their fitting procedure. The modelled ratios are plotted in purple for the fit of the frequencies and in cyan for the fit of the ratios. The bump at the right of the plot for the r_{01} and r_{10} ratios is likely due to surface activity during the measurement.

the envelope. Hence, Y_0 is mainly indirectly constrained by the non-seismic observables (i.e. the metallicity, the effective temperature, and the luminosity), which are limited and have a conservative precision as they come from a survey. Consequently, Y_0 is weakly constrained and has a large uncertainty, as shown in Appendix C. We still note that the primordial helium mass fraction is contained within the first sigma and that the observed [Fe/H] has a large uncertainty as well. The value of Y_0 for the fit of the ratios is slightly higher than Y_p, but the same argument applies. Therefore, the large uncertainty on the helium mass fraction just indicates that it is not possible to precisely constrain this quantity with the current data. We remark that Kepler-93

Table 2. Physical ingredients of the different models.

Name	Mass ($M_\odot$)	Radius ($R_\odot$)	Age (Gyr)	X_0	$(Z/X)_0$	Opacities	Abundances	Diffusion	Convection
$Model_1$	0.923 ± 0.024	0.923 ± 0.017	6.79 ± 0.26	0.753 ± 0.14	0.0130 ± 0.0017	OPAL	AGSS09	Paquette	MLT
$Model_2$	0.907 ± 0.017	0.918 ± 0.006	6.78 ± 0.23	0.744 ± 0.14	0.0123 ± 0.0017	OPAL	AGSS09	Paquette	MLT
$Model_3$	0.907 ± 0.021	0.918 ± 0.007	6.65 ± 0.31	0.744 ± 0.17	0.0123 ± 0.0026	OPAL	AGSS09	Paquette	MLT + OV1
$Model_4$	0.907 ± 0.021	0.918 ± 0.007	6.65 ± 0.31	0.744 ± 0.17	0.0123 ± 0.0026	OPAL	AGSS09	Paquette	MLT + OV2
$Model_5$	0.908 ± 0.021	0.918 ± 0.007	6.60 ± 0.32	0.743 ± 0.17	0.0123 ± 0.0027	OPAL	AGSS09	Paquette	MLT + OV3
$Model_6$	0.908 ± 0.021	0.918 ± 0.007	6.65 ± 0.38	0.743 ± 0.17	0.0123 ± 0.0026	OPAL	AGSS09	Paquette	MLT + OV4
$Model_7$	0.907 ± 0.021	0.918 ± 0.007	6.68 ± 0.32	0.744 ± 0.17	0.0122 ± 0.0027	OPAL	AGSS09	Paquette + DT1	MLT
$Model_8$	0.907 ± 0.021	0.918 ± 0.007	6.72 ± 0.33	0.744 ± 0.17	0.0122 ± 0.0027	OPAL	AGSS09	Paquette + DT2	MLT
$Model_9$	0.914 ± 0.021	0.920 ± 0.007	6.67 ± 0.32	0.743 ± 0.16	0.0149 ± 0.0032	OPAL	GN93	Paquette	MLT
$Model_{10}$	0.905 ± 0.022	0.917 ± 0.007	6.51 ± 0.36	0.745 ± 0.18	0.0127 ± 0.0027	OPLIB	AGSS09	Paquette	MLT
$Model_{11}$	0.909 ± 0.021	0.918 ± 0.007	6.68 ± 0.31	0.743 ± 0.17	0.0125 ± 0.0027	OPAL	AGSS09Ne	Paquette	MLT
$Model_{12}$	0.907 ± 0.021	0.918 ± 0.007	6.72 ± 0.32	0.743 ± 0.17	0.0123 ± 0.0026	OPAL	AGSS09	Paquette + PartIon	MLT

Notes. The errors are statistical errors. $Model_1$ is based on the fit of the individual frequencies with AIMS and $model_2$ on the fit of the frequency ratios. The remaining models are the results of the Levenberg minimisation. $Models_{3-6}$ have an overshoot of $\alpha_{ov} = 0.05$, 0.10, 0.15, and 0.20.

and low-metallicity targets more generally are interesting in this aspect as excellent spectroscopic and seismic data would allow indicating possible inconsistencies in the stellar models based on the predicted initial helium mass fraction.

The goal of the global minimization was to restrict the parameter space to start varying the physical ingredients and locally explore the parameter space in a more detailed way. We will also be able to test the impact of different prescriptions to estimate the surface effects.

2.2. Local minimization and impact of the physical ingredients

In this section, we test a wide range of prescriptions for the physical processes acting in the star, focussing first on the impact of the abundances. For this purpose, we tested the GN93 (Grevesse & Noels 1993), the AGSS09 (Asplund et al. 2009), and the AGSS09Ne (AGSS09 with the Neon revised according to Landi & Testa 2015; Young 2018) abundances. Then, we investigated the impact of the opacities by considering the OPAL (Iglesias & Rogers 1996) and the OPLIB (Colgan et al. 2016) opacities. The impact of a turbulent diffusion (DT; Proffitt & Michaud 1991) was also tested. The turbulent coefficient has the form

$$D_{turb} = D \left(\frac{\rho_{bcz}}{\rho(r)} \right)^n, \tag{2}$$

where D and n are free parameters, ρ_{bcz} is the density at the base of the convective zone, and $\rho(r)$ is the density profile. We considered two sets of coefficients, from Buldgen et al. (2017) and Proffitt & Michaud (1991), respectively. The first set is given by $D_1 = 50$ and $n_1 = 2$, and the second set by $D_2 = 7500$ and $n_2 = 3$. The mixing-length parameter α_{MLT} is one of the free variables. The remaining physical ingredients are the same as for the global minimization. A summary of the models we used is listed in Table 2. A graphical representation of Table 2 is displayed in Fig. 4, with the PLATO precision requirements (light orange band) and the final 1σ-interval (cf. Table 3) of the optimal stellar parameters of Kepler-93 (dark orange band).

The Levenberg-Marquardt algorithm is known to have difficulties in properly estimating the uncertainty. It finds the minimum and only then estimates the errors based on the steps that led to this optimal solution. Two problems arise with this procedure. First, the minimum can be local and the errors are underestimated in this case and second, if the steps become too small,
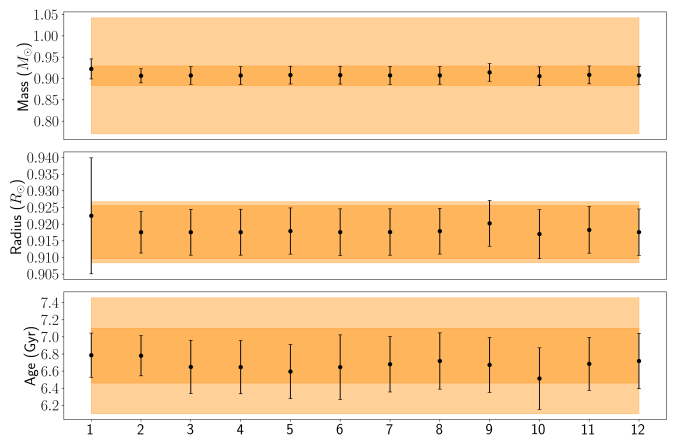
Fig. 4. Graphical visualisation of Table 2. The numbers i of the x-axis should be read as *model i*. *From top to bottom*: mass, radius, and age of the different models. The dark orange band indicates the final 1σ-interval (cf. Table 3) and the light orange band the precision requirements of PLATO (15% in mass, 1–2% in radius, and 10% in age). The optimal stellar parameters are well within the PLATO precision requirements.

the inversion of the Hessian matrix may fail and output overestimated uncertainties. In order to avoid these problems, we estimated with AIMS and its robust error estimation, the uncertainties expected with the same set of constraints and adapted our steps to reproduce them. We did not use r_{01} (nor r_{10}) as constraints in the Levenberg-Marquardt minimisation. The sole fit of r_{02}, the inverted mean density, and the non-seismic constraints are able to reproduce all the ratios well, as shown in Fig. 5. In addition, including them would make the algorithm unstable. The error on the radius is not provided by the Levenberg algorithm because it is not one of the optimised variables, but it can be estimated using a rule of thumb. The relative uncertainty on the radius is about one-third of the uncertainty of the mass because the inverted mean density is included in the constraints. This was observed by Buldgen et al. (2019a) for Kepler-444, and the same behaviour also appears with Kepler-93 in the AIMS results. We stress that the errors provided by the Levenberg-Marquardt minimisation are not considered robust. However, this is not a problem because we only used the results from the local minimisation to estimate the systematics due to the physical ingredients, and our final value are based on the model from AIMS, whose error estimation procedure is far more
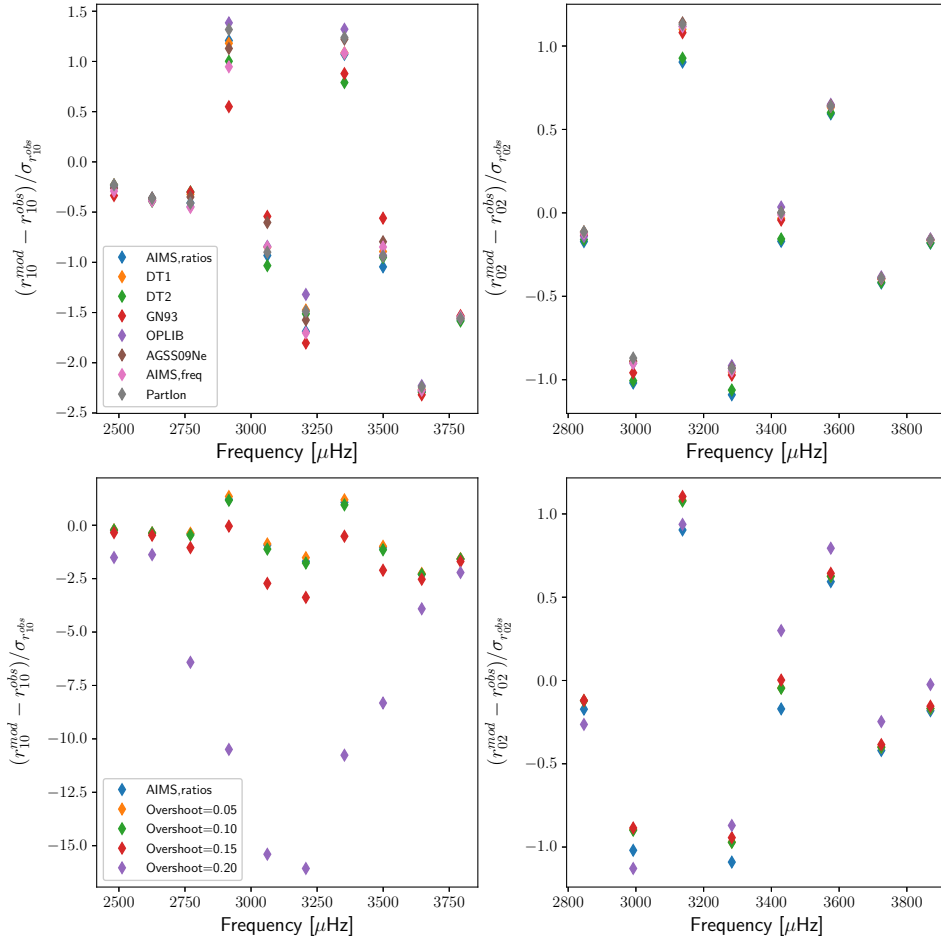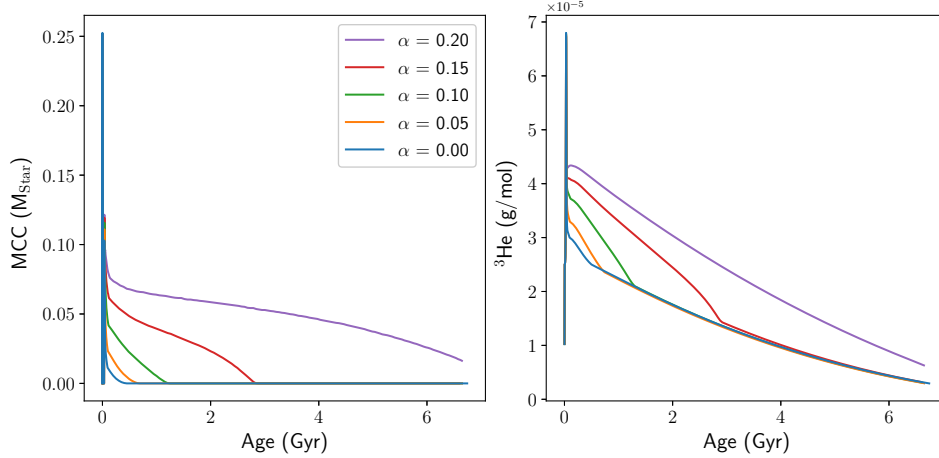
Fig. 5. Comparison of the models with different physical ingredients. *Upper panel*: comparison of the r_{10} (*left*) and r_{02} (*right*) frequency ratios obtained by varying the physical ingredients and without overshoot. The model with the GN93 abundances stands out slightly. *Lower panel*: comparison of the r_{10} (*left*) and r_{02} (*right*) frequency ratios obtained by varying the overshoot parameter. The model labelled AIMS, ratios is without overshoot. There is no visible difference between the blue and orange symbols in the *lower left panel*. Orange and green symbols are also largely superimposed in the *lower right panel*.

reliable and robust. We also note that the α_{MLT} parameter, which is a free variable in the minimisation process and without constraining prior interval, stayed close to the solar calibrated value $\alpha_{\mathrm{MLT},\odot} \simeq 2.05$ (see Sect. 2.1 for the associated set of physical ingredients). We remark that we used a VAL-C atmosphere. The estimated uncertainty for this quantity is about 0.1, and the standard deviation of the sample is 0.02, which is well below one sigma. The fact that α_{MLT} stays close to the solar calibrated value indicates that we cannot constrain this quantity with our data.

A comparison of the r_{10} and r_{02} frequency ratios obtained with the different models of this work without overshoot is shown in the upper panel of Fig. 5. These results are relatively close to each other, indicating that a change in physical ingredients does not have a significant impact. We still remark that the model with the GN93 abundances stands out slightly. With theses abundances, we have a change in the initial chemical composition, which modifies the behaviour of the sound speed in the radiative zone. This will change the modelled stellar radius, and consequently, the ratios. Figure 5 is to be considered with caution. We display the quantity $(r_{xy}^{\mathrm{mod}} - r_{xy}^{\mathrm{obs}})/\sigma_{xy}^{\mathrm{obs}}$, which boosts the differences between the observations and the modelled ratios, especially if the precision of the observed ratio is very high. Figure 3 shows, however, that the models without overshoot reproduced the observed ratios well.

For Kepler-444 and HD 203608, which are targets with masses and metallicities similar to those of Kepler-93, it was found that a transitory convective formed during their evolution, and its trace is still visible in the observed ratios. In the case of Kepler-444, the survival of the convective core for a significant part of the stellar lifetime showed an impact on the observed frequencies and ratios (Buldgen et al. 2019a). Deheuvels et al. (2010) found strong evidence that the convective core of HD 203608 survived until the present. Therefore, we investigated the survival of the convective core of Kepler-93 to understand whether this effect should be taken into account in the modelling. The evolution and lifetime of a convective core are linked to the ^{3}He/H ratio. More precisely, the critical point is the temperature sensitivity of the out-of-equilibrium ^{3}He burning, which concentrates the energy generation in a smaller region and hence increases the radiative gradient. As illustrated in the right panel of Fig. 6, without overshooting, this ratio quickly reaches an equilibrium value, and consequently, the ppI chain reaches equilibrium. In this case, the radiation is sufficient to evacuate the energy flux. With the consideration of an overshoot, which brings more ^{3}He into the central regions, its out-of-equilibrium burning will last longer. Because the out-of-equilibrium ^{3}He burning temperature is too high for radiation to evacuate the heat, the lifetime of the convective core is extended, and it can remain during the

Fig. 6. *Left*: comparison of the evolution of the mass of the convective core (MCC) with different overshooting efficiencies. The lilac model with a strong overshoot does not reproduce the observed frequency ratios. Hence, a convective core is not expected to survive until the present. *Right*: comparison of the evolution of central ^{3}He abundance with different overshoots.

main sequence (Roxburgh 1985). In the lower panel of Fig. 5, we tested several overshoot regimes. The models with low overshoot do not depart from the models with no overshoot, while the models with strong overshoot do not reproduce the observed ratios. The lifetime of the convective core for Kepler-93 is plotted in the left panel of Fig. 6. Without overshoot, the convective core disappears almost instantaneously. Because the model with strong overshoot does not reproduce the observed ratios, the lifetime of a convective core is not expected to exceed 3 Gyr. Hence, no trace of a convective core is visible in the seismic data at the current age of the star, and the analysis is complete without explicit consideration of an overshoot in the modelling.

3. Inversions for the stellar structure

In this section, we perform inversions of the CLES models computed in the previous part to improve the robustness of our analysis. Inversions are defined in such a way that they do not rely strongly on the choice of physical ingredients in the model and can thus extract additional information from the asteroseismic data in a quasi-model-independent way. Several prescriptions for the surface effects were tested by correcting the individual frequencies before the inversion or implementing them in the inversion. These inversions provide estimates of so-called indicators. Several of them are available in the literature (Reese et al. 2012; Buldgen et al. 2015a,b, 2018), but we limit ourselves to the mean density inversions. The τ indicator is indeed too sensitive to surface effects and the error on the correction predicted by the inversion is too high to extract meaningful information with this quantity. In addition, some of the indicators that require numerous quadrupole modes (e.g. S_{core} in Buldgen et al. 2018) are not compatible with the limited number of observed quadrupole modes for Kepler-93.

3.1. Theoretical considerations

The structure inversion equation is based on the analysis of the perturbation of the equation of motion describing the evolution of the displacement vector and considering only the linear terms. This approach is motivated by the work of Lynden-Bell & Ostriker (1967) and their predecessors (see e.g. Chandrasekhar 1964; Chandrasekhar & Lebovitz 1964; Clement 1964), who showed that the equation of motion fulfils a vari-

ational principle. In our case, the frequency perturbation is directly related to the structural perturbation and can be rewritten in the usual form (Dziembowski et al. 1990),

$$\frac{\delta \nu^{n,l}}{\nu^{n,l}} = \int_0^R K_{a,b}^{n,l} \frac{\delta a}{a} dr + \int_0^R K_{b,a}^{n,l} \frac{\delta b}{b} dr + O(\delta^2), \tag{3}$$

with ν the oscillation frequency, a and b two structural variables, $K_{a,b}^{n,l}$ and $K_{b,a}^{n,l}$ the structural kernels and using the definition

$$\frac{\delta x}{x} = \frac{x_{\text{obs}} - x_{\text{ref}}}{x_{\text{ref}}}. \tag{4}$$

The index *ref* stands for reference and *obs* stands for observed. Then, the idea is to invert Eq. (3) and compute the indicator t given the observed frequency differences.

The treatment of surface regions is quite approximative in Eq. (3), requiring the surface effects to be modelled by an additional empirical term, denoted $\mathcal{F}_{\text{Surf}}$. In the literature (Ball & Gizon 2014; Sonoi et al. 2015), this term is considered to be slowly varying with frequency and is determined in an empirical way. Ball & Gizon (2014) proposed a correction of the form

$$\delta \nu = \left(a_{-1} \left(\frac{\nu}{\nu_{\text{ac}}} \right)^{-1} + a_3 \left(\frac{\nu}{\nu_{\text{ac}}} \right)^3 \right) / \mathcal{I}, \tag{5}$$

where $\delta \nu$ is the estimated correction[1], $\mathcal{I}$ is the mode inertia, and a_{-1} and a_3 are two coefficients to be added in the optimisation procedure. The acoustic cut-off ν_{ac} is computed using the scaling relation,

$$\frac{\nu_{\text{ac}}}{\nu_{\text{ac},\odot}} = \frac{g}{g_\odot} \left(\frac{T_{\text{eff}}}{T_{\text{eff},\odot}} \right)^{-\frac{1}{2}}, \tag{6}$$

with $g_\odot = 27\,400\,\text{cm s}^{-2}$, $T_{\text{eff},\odot} = 5772\,\text{K}$, and $\nu_{\text{ac},\odot} = 5000\,\mu\text{Hz}$. On the other hand, the approach of Sonoi et al. (2015) is based on the stellar properties and does not require new optimisation coefficients,

---

[1] $\delta \nu = \nu_{\text{WSC}} - \nu_{\text{NSC}}$, where WSC stands for a correction for surface effects, and NSC stands for no correction for surface effects. By convention in this section, the frequency without index is the frequency without correction for surface effects.

$$\frac{\delta\nu}{\nu_{\max}} = \alpha\left(1 - \frac{1}{1 + \left(\frac{\nu_{\mathrm{WSC}}}{\nu_{\max}}\right)^{\beta}}\right), \tag{7}$$

where α and β can be determined from the surface gravity and effective temperature,

$$\log|\alpha| = 7.69\log T_{\mathrm{eff}} - 0.629\log g - 28.5 \tag{8}$$

$$\log\beta = -3.86\log T_{\mathrm{eff}} + 0.235\log g + 14.2. \tag{9}$$

The coefficients α and β could be treated as free variables in the optimisation process. However, because this correction is empirical, is it not worthwhile doing this. The frequency of maximum power $\nu_{\max} = 3366\,\mu\mathrm{Hz}$ is taken from Davies et al. (2016).

In order to perform the inversion, we chose the Substractive Optimally Localized Averages (SOLA) approach (Pijpers & Thompson 1994), which is an adaptation of the OLA approach of Backus & Gilbert (1968, 1970). Methods that take the non-linearities into account can also be found in the literature (Roxburgh 2002; Roxburgh & Vorontsov 2002a,b; Appourchaux et al. 2015) and might be a good complement to confirm the results of this work. The SOLA method consists of minimising of the following cost function for a given indicator t:

$$\mathcal{J}_t(c_i) = \int_0^1 \left(\mathcal{K}_{\mathrm{avg}} - \mathcal{T}_t\right)^2 \mathrm{d}x + \beta \int_0^1 \mathcal{K}_{\mathrm{cross}}^2 \mathrm{d}x + \lambda\left[2 - \sum_i c_i\right]$$
$$+ \tan\theta\frac{\sum_i(c_i\sigma_i)^2}{\langle\sigma^2\rangle} + \mathcal{F}_{\mathrm{Surf}}(\nu), \tag{10}$$

where the averaging and cross-term kernels are related to the structural kernels,

$$\mathcal{K}_{\mathrm{avg}} = \sum_i c_i K_{a,b}^i \tag{11}$$

$$\mathcal{K}_{\mathrm{cross}} = \sum_i c_i K_{b,a}^i. \tag{12}$$

The variables β and θ are trade-off parameters to adjust the balance between the amplitudes of the different terms during the fitting. The idea is to reduce the contribution of the cross-term and of the observational errors on the individual frequencies while providing a good fit of the target function $\mathcal{T}_t$. A good fit of the target function by the averaging kernel ensures an accurate inversion result. Moreover, $\langle\sigma^2\rangle = \sum_i^N \sigma_i^2$ is defined, with N the number of observed frequencies, and σ_i the uncertainties of the *relative* frequency differences. The inversion coefficients are denoted with c_i, and λ is a Lagrange multiplier. The surface term $\mathcal{F}_{\mathrm{Surf}}(\nu)$ has to be treated with caution. It allows taking the surface effects into account, but at the expense of the fit of the target function.

3.2. Mean density inversions

Mean density inversions were formalised in Reese et al. (2012). They are a well-tested method (Reese et al. 2012; Buldgen et al. 2015a) that has been applied to various cases (Buldgen et al. 2016a,b, 2019a; Salmon et al. 2021) and that can efficiently extract key information from asteroseismic observations in a quasi-model-independent way. In addition, they do not necessarily require quadrupole modes, which are more difficult to observe.

The form of the target function is motivated by considering the mass difference between the star and the reference model and deducing from it the relative difference in mean density,

$$\frac{\delta\bar{\rho}}{\bar{\rho}} = \int_0^1 4\pi x^2 \frac{\rho}{\rho_{\mathrm{R}}} \frac{\delta\rho}{\rho} \mathrm{d}x, \tag{13}$$

where $\rho_{\mathrm{R}} = \frac{M}{R^3}$ is used for the non-dimensionalisation. M is the stellar mass, R is its radius, and $x = \frac{r}{R}$ is the normalized radius. It follows that the target function of the mean density inversion is given by

$$\mathcal{T}_{\bar{\rho}} = 4\pi x^2 \frac{\rho}{\rho_{\mathrm{R}}}. \tag{14}$$

The frequencies of the reference models for the inversion were computed without surface effects. We added them a posteriori, either by correcting the frequencies of the reference models and then performing the inversion or by implementing them in the SOLA cost function. We used four prescriptions to test their impact. The first prescription, labelled *no surface corr.*, was to carry out the inversion without surface effects. It is an extreme case that gives a lower bound for the mean density. The second, labelled *AIMS+BG 2014*, was to use the Ball & Gizon (2014) coefficients obtained with AIMS and the fitting of the individual frequencies. The third prescription, labelled *Sonoi 2015*, was to correct the modelled frequencies with the Sonoi et al. (2015) procedure. For these three prescriptions, inversions were carried out without the term for the surface correction in the SOLA cost function. The last prescription, labelled *SOLA+BG 2014*, was to implement the Ball & Gizon (2014) correction in the $\mathcal{F}_{\mathrm{Surf}}$ term in the SOLA cost function. The downside of this approach is that it added two free variables to the minimisation. Consequently, the target function was less well reproduced by the averaging kernel, and the uncertainty on the inverted mean density was significantly higher.

The results of the inversions for the different models are displayed in Fig. 7. This plot shows that it is necessary to take the surface effects into account. All the uncorrected models are biased and lie left of the plot (dark blue points). The results for which the surface effects were implemented are not entirely bias-free either. Figure 8 shows that the model without surface effects tends to overestimate the observed high frequencies, where the contribution of these surface effects is stronger, while the frequencies estimated taking the surface effects into account tend to slightly underestimate the frequencies.

The revised stellar parameters are listed in Table 3. The mass, radius, and age come from the fit of the ratios with AIMS. The uncertainties are the addition of the statistical uncertainties provided by AIMS and the systematic errors due to the choice of physical ingredients and of observables[2] estimated with the standard deviation of the models listed in Table 2. We did not include the models with overshoot in the standard deviation as they predicted frequency ratios that agreed even less with the observations. The standard deviation is therefore based on models 1−2 and 7−12. In order to provide a consistent estimate of the stellar mean density, we computed the weighted mean (with weights $w_i = 1/\sigma_i^2$) of the inversion results with and without surface effects, because the true value is expected to lie in-between. The weighted mean and the median are almost equal. The error was chosen in such a way that most of the models lie within the error interval. This conservative estimation of the uncertainty still leads to a high precision on the mean density. The precision is about 0.2%.

---

[2] The observables refer to the seismic constraints used in the fit: individual frequencies, or frequency ratios.
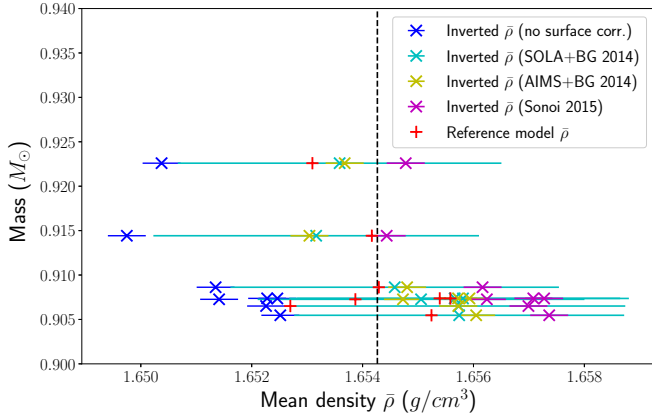
Fig. 7. Mean density inversions results. The vertical dashed black line is the weighted mean. The four prescriptions for the surface effects are described in detail after Eq. (14). no surface corr. corresponds to the first prescription, AIMS+BG 2014 to the second, Sonoi 2015 to the third, and SOLA+BG 2014 to the last prescription.

Table 3. Revised stellar parameters of Kepler-93.

Mean density (g cm^{-3})	Mass ($M_\odot$)	Radius ($R_\odot$)	Age (Gyr)
1.654 ± 0.004	0.907 ± 0.023	0.918 ± 0.008	6.78 ± 0.32

Notes. The quoted errors include the systematics due to the choice of the physical ingredients for the mass, age and radius and the impact of surface effects and model-dependence in the inversion for mean density.

A consistency test was then conducted. A mass range was deduced from the mean density and using the Stefan-Boltzmann law to obtain the radius from the spectroscopic constraints,

$$M_{SB} = \frac{4\pi}{3}\bar{\rho}\left(\frac{L}{4\pi\sigma_{SB}T_{eff}^4}\right)^{3/2} \qquad (15)$$

$$\sigma_{M_{SB}} = M_{SB}\sqrt{\left(\frac{\sigma_{\bar{\rho}}}{\bar{\rho}}\right)^2 + \left(\frac{3}{2}\frac{\sigma_L}{L}\right)^2 + \left(6\cdot\frac{\sigma_{T_{eff}}}{T_{eff}}\right)^2}. \qquad (16)$$

This mass range is based on the spectroscopic constraints and on the mean density obtained with the inversions. It is therefore quasi-independent of the forward modelling. We obtained $M_{SB} = 0.925 \pm 0.110\,M_\odot$. All the mass estimates of our work and of the literature lie within this mass range, which is consistent with our expectation. The precision on M_{SB} is limited by the error on the effective temperature. The best estimate of the effective temperature in the literature was computed within a survey and might therefore be improved with a detailed spectroscopic analysis of Kepler-93. This point is crucial for improvements, because the estimate of the effective temperature also affects the estimated stellar luminosity. For example, if the error on the effective temperature were 50 K instead of 100 K, the error on M_{SB} might be reduced by about 35%.

The stellar parameters are consistent with the literature values. Silva Aguirre et al. (2015) also investigated the impact of input physics, but they focussed on the abundances and the mixing-length parameter. In our work, we tested many more physical ingredients (abundances, opacities, turbulent diffusion, overshoot, etc.). In addition, Silva Aguirre et al. (2015) considered a sample of 33 targets and estimated the systematics based
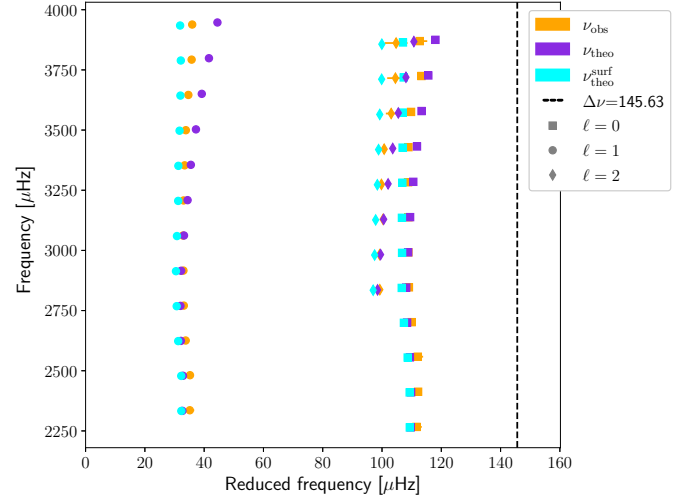
Fig. 8. Echelle diagram of the result of AIMS with the fit of the ratios. The inverted mean density was part of the constraints. The comparison between the results with (cyan) and without (purple) correction for the surface effect is shown. The Ball & Gizon (2014) correction was chosen for this plot, but the effect is similar with another prescription for the surface effects.

on median values, while we conducted a detailed analysis of a single star. Because their sample contains F-type stars and stars massive enough to have a convective core, their uncertainties are therefore likely overestimated in the case of solar-type stars, such as Kepler-93. This especially explains why they quote a precision on the age that is significantly lower than ours. They did not use mean density inversions either, which limits the precision on the mean density in their forward modelling. Finally, we remark that our detailed analysis of Kepler-93 provided stellar parameters that are well within the precision requirements for the PLATO mission.

3.3. Revision of the planetary parameters

Based on the improvement of the precision on the stellar parameters, we provide in Table 4 a revision of the planetary parameters of Kepler-93b.

The planet induces a RV signal on the host star, which allows determining the planetary mass (Cumming et al. 1999),

$$K = \left(\frac{2\pi G}{P}\right)^{1/3}\frac{M_p}{(M_\star + M_p)^{2/3}}\frac{\sin i}{\sqrt{1-e^2}}, \qquad (17)$$

where K is the RV amplitude, G is the Newtonian gravitational constant, P is the orbital period of the planet, $M_\star$ is the host star mass, M_p is the planet mass, i is the inclination, and e is the orbital eccentricity. As in Dressing et al. (2015), we assumed that $e = 0$ because they found that a non-zero eccentricity did not provide a better fit in their analysis. Although this equation possesses an exact solution using an appropriate substitution and Cardano's formula, it is numerically more stable to use a Monte Carlo procedure to estimate the error on the planetary mass. At first, we investigated the impact of the precision on the stellar mass by fixing the other parameters. We found that the improvement of a factor two leads to a factor two on the precision of the planet mass. However, the RV amplitude is not error-free and completely dominates the uncertainty on the planetary mass. The main contributor to the error on the planet mean density is the planet mass. Consequently, the precision on this quantity

Table 4. Revised planetary parameters of Kepler-93b.

Parameter	Value with 1σ error	Reference
Transit and orbital parameters		
Orbital period P (days)	$4.72673978 \pm 9.7 \times 10^{-7}$	1
$R_{\rm p}/R_{\star}$	0.014751 ± 0.000059	1
$a/R_{\star}$	12.496 ± 0.015	1
Inclination i (deg)	89.183 ± 0.044	1
Orbital eccentricity e	0 (fixed)	2
RV semi-amplitude K (m s^{-1})	1.63 ± 0.27	2
Planetary parameters		
$R_{\rm p}$ ($R_{\oplus}$)	1.478 ± 0.014	3
$M_{\rm p}$ ($M_{\oplus}$)	4.01 ± 0.67	3
$\rho_{\rm p}$ (g cm^{-3})	6.84 ± 1.16	3
$\log g_{\rm p}$ (cgs)	3.256 ± 0.074	3
a (AU)	0.0533 ± 0.0005	3

Notes. The uncertainties of the values revised in this work include the systematics found for the stellar parameters.
References. (1) Ballard et al. (2014); (2) Dressing et al. (2015); (3) this work.

remains unchanged. This issue will be less important for PLATO or TESS targets observed in the southern hemisphere, for which the RV follow-up will be more thorough.

The gain in precision on the stellar radius is more significant, especially as it improves the uncertainty on the planetary radius and orbital distance by about 25% and 27% with respect to the values of Dressing et al. (2015).

4. Orbital evolution of Kepler-93b

The detailed asteroseismic characterisation of the system presented in the previous sections, which provided very precise stellar parameters and revised planetary parameters, allows us to proceed with studying the orbital evolution of Kepler-93b. In this section, we investigate in particular whether the gravitational tidal interaction between the planet and the host star played a significant role in the past history of the system. Consequently, we estimate the X-ray and EUV fluxes received by the planet during its potential orbital motion.

In this context, the availability of precise parameters (such as the age) is crucial in order to discard past evolutionary scenarios that would prevent us from reproducing the current status of the system within the uncertainties of the fundamental quantities. Therefore we started our study by computing a model of Kepler-93 by means of the CLES stellar evolution code, using the stellar parameters derived above as input and constraints for the model.

In order to follow the evolution of the planetary system, we coupled the stellar model to our orbital evolution code (Privitera et al. 2016; Rao et al. 2018; Pezzotti et al. 2021), taking the exchange of angular momentum between the star and the orbit into account after the protoplanetary disk has dissipated. With this approach, we can test whether dynamical and/or equilibrium tides have significantly impacted the orbit of the planet. Dynamical tides are mainly efficient during the PMS phase when the host star rotates faster, while equilibrium tides take over at the later stages of the evolution. The physics included in the orbital evolution code is described in Rao et al. (2018) and Pezzotti et al. (2021). Estimates of the mass loss from planetary atmospheres are provided following the formalism of the Jeans or hydrodynamic escape regimes, depending on the properties of the planetary system considered.

The rotational history of Kepler-93 is unknown. We therefore considered three different values for the initial surface rotation rate that are representative of slow ($\Omega_{\rm in} = 3.2 \times \Omega_{\odot}$), medium ($\Omega_{\rm in} = 5 \times \Omega_{\odot}$), and fast rotators ($\Omega_{\rm in} = 18 \times \Omega_{\odot}$), as deduced from surface rotation rates of solar-type stars observed in open clusters at different ages (Eggenberger et al. 2019). A disk lifetime $\tau_{\rm dl} = 6$ Myr was adopted for medium and slow rotators, and while $\tau_{\rm dl} = 2$ Myr was adopted for the fast rotator. During the disk-locking timescale, the surface rotation of the host star was assumed to remain constant. After disk dispersal, the star was assumed to rotate as a solid body. This assumption receives some support from the rotational profile deduced for the Sun from helioseismology (see e.g. Kosovichev 1988; Brown et al. 1989; Elsworth et al. 1995; Kosovichev et al. 1997; Couvidat et al. 2003), which is flat in most of the envelope and the nearly uniform internal rotation of solar-like main-sequence stars derived from seismic analysis (see e.g. Lund et al. 2014; Benomar et al. 2015).

For the magnetic braking of the stellar surface, we refer to the formalism of Matt et al. (2015, 2019), for which the torque is given by

$$\frac{{\rm d}J}{{\rm d}t} = \begin{cases} -T_{\odot}\left(\dfrac{R_{\star}}{R_{\odot}}\right)^{3.1}\left(\dfrac{M_{\star}}{M_{\odot}}\right)^{0.5}\left(\dfrac{\tau_{cz}}{\tau_{cz\odot}}\right)^{p}\left(\dfrac{\Omega}{\Omega_{\odot}}\right)^{p+1}, & \text{if } ({\rm Ro} > {\rm Ro}_{\odot}/\chi), \\ -T_{\odot}\left(\dfrac{R_{\star}}{R_{\odot}}\right)^{3.1}\left(\dfrac{M_{\star}}{M_{\odot}}\right)^{0.5}\chi^{p}\left(\dfrac{\Omega}{\Omega_{\odot}}\right), & \text{if } ({\rm Ro} \leq {\rm Ro}_{\odot}/\chi), \end{cases}$$
(18)

where $R_{\star}$ and $M_{\star}$ are the radius and the mass of the stellar model, and $R_{\odot}$ and $M_{\odot}$ are the radius and the mass of the Sun. The convective turnover timescale is indicated as τ_{cz}, and Ro is the Rossby number, defined as the ratio of the stellar rotational period and the convective turnover timescale (Ro $= P_{\star}/\tau_{cz}$). The term $\chi \equiv {\rm Ro}_{\odot}/{\rm Ro}_{\rm sat}$ indicates the critical rotation rate for stars with given $\tau_{cz}/\tau_{cz_{\odot}}$, defining the transition from the saturated to the unsaturated regime. Here we took $\chi = 10$ as in Matt et al. (2015) and Eggenberger et al. (2019). The exponent p was taken equal to 2.3, and the constant $T_{\odot}$ was calibrated in order to reproduce the solar surface rotation rate (Eggenberger et al. 2019).

In the top panel of Fig. 9, we present the evolution of the surface rotation rates computed for Kepler-93, starting from the dispersal of the protoplanetary disk until the current age of the system. We also show the evolution of the surface rotation rate of a super-slow rotator ($\Omega_{\rm in} = \Omega_{\odot}$). While such a rotator is less representative of the distribution of surface rotation rates observed for stars in open clusters at different ages, we include it in our study, because we are interested in considering its impact on the evaporation of the planetary atmosphere (see below). Unfortunately, there is no precise estimate of the surface rotation rate of Kepler-93 with which we might compare our models. Mazeh et al. (2015) provided a value of the rotational period of the star, but they flagged the detection as inconsistent in different quarters and as not robust. Suto et al. (2019) also estimated a rotation period for Kepler-93, but they considered this star to have no clear signal in its periodogram and flagged the period as unreliable. At the current age of the system, our models predict a value of the rotational period of $P_{\rm rot} = 33.7$ d.

In the bottom panel of Fig. 9, we show the XUV luminosity evolutionary tracks computed for fast (solid black line), medium (solid magenta line), slow (solid blue), and super-slow rotators (solid red line). Following the work by Tu et al. (2015), we computed the emission of the X-ray luminosity by recalibrating the
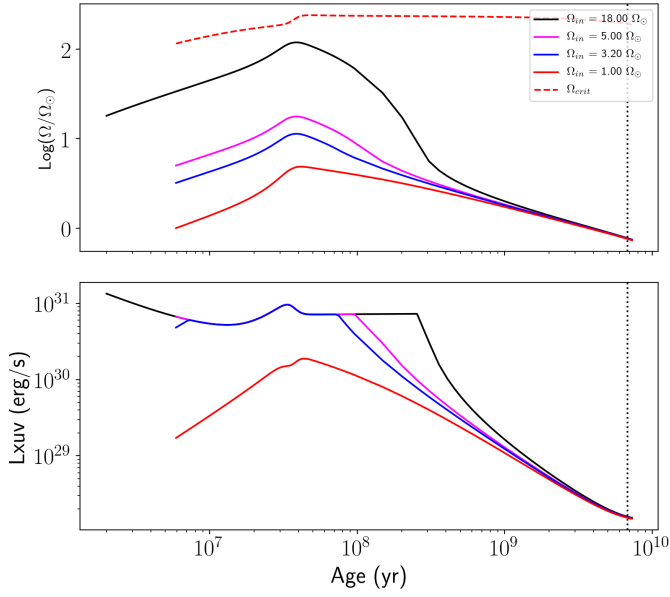
Fig. 9. *Top panel*: evolution of the surface rotation rate of Kepler-93, in case of fast rotator ($\Omega_{\rm ini} = 18 \times \Omega_\odot$, black solid line), medium rotator ($\Omega_{\rm ini} = 5 \times \Omega_\odot$, magenta solid line), slow rotator ($\Omega_{\rm ini} = 3.2 \times \Omega_\odot$, blue solid line) and super-slow rotator ($\Omega_{\rm ini} = \Omega_\odot$, red solid line). The red dashed line shows the critical velocity limit. The black-dotted vertical line indicates the age of the system. *Bottom panel*: XUV luminosity evolutionary tracks of Kepler-93, relatively to the different rotational histories considered.

prescription of Wright et al. (2011). Their prescription gives the ratio of the X-ray luminosity with respect to the bolometric luminosity of the star ($Rx = Lx/L_\star$) in saturated and unsaturated regimes, depending on the value of the Rossby number. To compute the EUV luminosity, we used the prescription of Sanz-Forcada et al. (2011). Only the super-slow rotator never enters the saturation regime, providing an XUV luminosity emission that occurs at globally lower magnitudes.

We started our computations by studying the impact of dynamical tides on the total change of the orbital distance. We first chose the current value of the orbital distance as initial input for our computations ($a_{\rm in} = 0.0533$ AU, Table 4) in order to test whether we reproduced the position of the planet at the age of the system. For the planetary mass, we took the maximum allowed value for Kepler-93b within the error bar ($M_{\rm in} = 4.68\,M_\oplus$, Table 4) and considered it to remain constant during its evolution. In order to maximise the impact of dynamical tides, we considered Kepler-93 to have started the evolution as a fast rotator, namely with an initial surface rotation rate $\Omega_{\rm in} = 18 \times \Omega_\odot$. As a result of this simulation, we find that tides do not play a significant role in shaping the architecture of the system, leaving the orbit of the planet unperturbed.

We note that the relatively low mass ratio of the planet and the star, together with the high value of the initial orbital distance, plays a significant role in determining the efficiency of tides. We investigated these points in more detail with some additional computations in order to verify how sensitively this result depends on the values of the initial planetary mass and orbital distance. Firstly, we studied the impact of changing the value of the initial orbital distance. We computed orbital evolutions for a planet with a mass fixed to the maximum allowed value for Kepler-93b ($M_{\rm in} = 4.68\,M_\oplus$) with a semi-major axis smaller than 0.0533 AU. In the top panel of Fig. 10, we present the orbital evolutions corresponding to different values of the semi-major
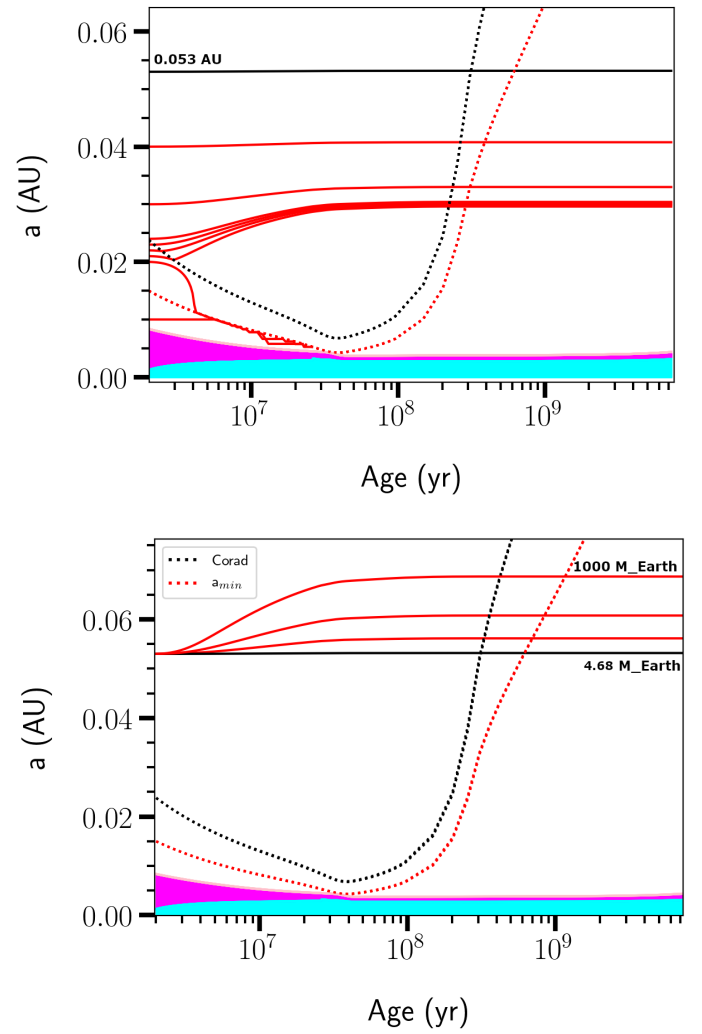
Fig. 10. *Top panel*: orbital evolution of a planet having a mass fixed at the maximal value allowed for Kepler-93b ($M_{\rm in} = 4.68\,M_{\rm Earth}$), for different values of the initial orbital distance: $a_{\rm in} = 0.01, 0.02, 0.021, 0.022, 0.023, 0.024, 0.03, 0.04$ and 0.053 AU. For initial orbital distances lower than ~ 0.023 AU, the planet would be rapidly engulfed by the host star. The initial surface rotation rate considered in both panels is $\Omega_{\rm in} = 18 \times \Omega_\odot$. *Bottom panel*: orbital evolution of a planet located at the same orbital distance of Kepler-93b (initial value fixed at $a_{\rm in} = 0.053$ AU), by considering different initial masses, the maximal value allowed for Kepler-93b ($M_{\rm in} = 4.68\,M_\oplus$, solid black line) and $M_{\rm in} = 100, 317, 1000\,M_\oplus$ (red solid lines). The magenta area represents the extension of the stellar convective envelope, while the cyan area represents the radiative core. The dotted black lines indicate the evolution of the corotation radii and the dotted red lines show the evolution of minimum orbital distance for dynamical tides to be active.

axis. We note that for values of $a_{\rm in}$ ranging between roughly $0.022-0.04$ AU, the orbits expand, while for $a_{\rm in} \leq 0.02$ AU, the planet is rapidly engulfed by the host star ($t_{\rm eng} \sim 3 \times 10^7$ Myr). Notably, none of the values of the semi-major axis we considered would reproduce the orbital distance of Kepler-93b at the age of the system. On the basis of this result, we would consider that the planet evolved at a fixed orbital distance (~ 0.0533 AU) after the dispersal of the protoplanetary disk. In a similar way, given the uncertainty on the measurement of the mass of Kepler-93b, we computed the orbital evolution of a planet at the same initial orbital distance as Kepler-93b, but with a higher initial mass. The bottom panel of Fig. 10 shows a slight increase in orbit only for

planets with an initial mass that is significantly higher than mass estimated for Kepler-93b within the error bars, namely only for $M_{pl} \gtrsim 100\,M_\oplus$. This result indicates that if Kepler-93b formed with a mass similar to its current value, tides did not play a crucial role in shaping the orbit of this planet.

We may ask whether Kepler-93b could have formed with an initial mass as high as $100\,M_\oplus$. This hypothesis would require that the planet experienced a substantial mass loss during its evolution in order to end up with only $\sim 4\,M_\oplus$ at the current age of the system. Such a planet might also have started the evolution with an orbital distance smaller than 0.0533 AU, because dynamical tides have been proven to expand the orbits of planets as massive as $100\,M_\oplus$ on timescales of the order of 30 Myr. We therefore recomputed the evolution of the planetary orbit, this time considering both the impact of the planetary mass loss through photoevaporation and mass loss through tides. We explored a range of initial orbital distances between 0.02 and 0.0533 AU for initial planetary masses $M_{in} = 100, 317$, and $1000\,M_\oplus$. Increasing the initial mass of the planet results in a more efficient impact of dynamical tides. Therefore, the maximum expansion of the orbit is obtained for a planet with $M_{in} = 1000\,M_\oplus$. We found that for some of the a_{in} values we considered, we were able to reproduce the current position of the planet. However, the mass loss obtained through photoevaporation is not strong enough to efficiently remove a significant percentage of the planetary mass. We find that for the initial masses we considered, the escape process occurs in Jeans escape regime conditions. This result was found for a star with an initial surface rotation rate $\Omega_{in} = 18\times\Omega_\odot$. Lower values of Ω_{in} would lead to similar outcomes, with a less efficient impact of tides. According to our results, it therefore seems unlikely that a planet like Kepler-93b formed with a mass high enough ($M_{in} \gtrsim 100\,M_\oplus$) for its orbit to be affected by stellar tides under the hypothesis that photoevaporation is the only process that induces mass loss from the planet.

The relatively high density estimated for Kepler-93b ($\rho = 6.84 \pm 1.15\,\mathrm{g\,cm}^{-3}$) would characterise this planet as a rocky world (Ballard et al. 2014; Dressing et al. 2015; Dorn et al. 2017). If an atmosphere surrounded the planet after the dispersal of the protoplanetary disk, it may have been lost at the early stages of the evolution through different processes, among which core-powered mass loss and/or evaporation due to high-energy stellar photons (Owen & Wu 2017; Ginzburg et al. 2018). Using photoevaporation, we aim at estimating the maximum initial mass of the planet (M_{max}) above which it would be able to retain a H/He-rich atmosphere after ~ 6.78 Gyr. We estimated the value of M_{max} by integrating backward in time the mass-loss rates obtained by using the energy-limited formula (Erkaev et al. 2007; Lecavelier Des Etangs 2007), for which we assumed a heating efficiency $\eta = 0.15$, and the hydro-based approximation of Kubyshkina et al. (2018). We computed the mass-loss rates for the fast and super-slow rotator. With the energy-limited formalism, we obtain that M_{max} is 9.4 and $5.4\,M_\oplus$ for the fast and super-slow rotator, respectively. In the case of the hydro-based approximation, we instead obtain the significantly higher value of $26.5\,M_\oplus$ for the fast rotator and $8.3\,M_\oplus$ for the slow rotator.

5. Conclusions

We carried out a detailed modelling of Kepler-93, a solar-like exoplanet host star that has been observed continuously for almost the whole duration of the nominal *Kepler* mission. We used a combination of seismic, spectroscopic and astrometric constraints to determine a best-fitting evolutionary model in Sect. 2 using a wide range of physical ingredients for the model.

This provided a clearer view of the contributions from modelling uncertainties in comparison to those of observational data. This first step of seismic forward modelling was supplemented in Sect. 3 by a seismic inversion of the mean density following Reese et al. (2012), where we tested the impact of model-dependence and surface effects on the inversion results. In Sect. 4 we used this model to study the orbital evolution under the effects of equilibrium and dynamical tides and the evaporation of the planetary atmosphere from the effects of the XUV flux.

Our final reported stellar parameters are $\bar{\rho}_\star = 1.654 \pm 0.004\,\mathrm{g\,cm}^{-3}$, $M_\star = 0.907 \pm 0.023\,M_\odot$, $R_\star = 0.918 \pm 0.008\,R_\odot$, and Age $= 6.78 \pm 0.32$ Gyr. They agree with previous determinations in the literature. The results of this detailed modelling were used to revise the planetary parameters of Kepler-93b, $\bar{\rho}_p = 6.84 \pm 1.16\,\mathrm{g\,cm}^{-3}$, $M_p = 4.01 \pm 0.67\,M_\oplus$, $R_p = 1.478 \pm 0.014\,R_\oplus$, $\log g_p = 3.256 \pm 0.074$, and $a = 0.0533 \pm 0.0005$ AU. Moreover, at the level of precision of the *Kepler* data, the spread obtained from varying the microphysical ingredients such as abundances, opacities, formalism of microscopic diffusion, and the inclusion of macroscopic transport at the base of the envelope in the form of turbulent diffusion does not significantly impact the mass and radius estimates. This is different from what was obtained in the case of Kepler-444 (Buldgen et al. 2019a), where the spread in mass and radius was significant at the level of precision of the Kepler data. However, the age determination of Kepler-93 can be significantly affected by a revision of the radiative opacities. In our case, switching from the OPAL (Iglesias & Rogers 1996) to the OPLIB (Colgan et al. 2016) opacities induced a change of $\approx 4\%$, which is not negligible at our reported precision. In the context of the solar modelling problem (see e.g. Basu & Antia 2008; Christensen-Dalsgaard 2021; Buldgen et al. 2019b, and references therein), this emphasizes that any revision of the opacities might impact the determined ages from stellar evolutionary models in the case of solar-like stars. Nevertheless, the overall spread in the fundamental stellar parameters is rather small and within the requirements of the PLATO mission (2% for the radius, 15% for the mass, and 10% for the age), even when variations in physical ingredients within the current limitations of the stellar models are taken into account.

While the effects of physical ingredients are more restricted in this specific case, the variations induced by choosing another set of seismic constraints are not. This is shown in Tables 1 and 2, where the use of individual frequencies as direct seismic constraints leads to a mass higher by about $\approx 1.5\%$ and to a radius larger by about $\approx 0.5\%$ than the one determined from the fit of the frequency ratios. This is in line with what was shown by Jørgensen et al. (2020), who tested various surface corrections in the seismic forward modelling using AIMS (although for red giant branch stars). In this respect, the choice of the seismic constraints for the modelling also affects the final set of parameters, at least at the precision aimed for in the context of the PLATO mission.

We also tested the possibility of the survival of a convective core coming from out-of-equilibrium ^{3}He burning at the beginning of the evolution, as seen in HD 203608 (Deheuvels et al. 2010). While Kepler-93 has a similar mass, it has a much higher metallicity [Fe/H] $= -0.18 \pm 0.1$ while HD 203608 has [Fe/H] $= -0.5 \pm 0.1$, thus the opacity in the deep layer could be different and thus impact the size and survival of the convective core. Using the r_{01} frequency ratios in Fig. 5, we can see that sustaining the out-of-equilibrium burning for about 3 Gyr leads to a worse agreement with seismic data. This implies that a convective core could not have been long lived in Kepler-93, unlike in Kepler-444 and HD 203608.

We computed stellar models of Kepler-93 using the stellar parameters derived from the asteroseismic characterisation as inputs and constraints. The rotational history of Kepler-93 is unknown. We therefore considered different values for the initial surface rotation rates that are representative of slow, medium and fast rotators. We studied the orbital evolution of Kepler-93b coupling the stellar models to our orbital evolution code, investigating the combined impact of dynamical or equilibrium tides and atmospheric photoevaporation. Exploring a range of initial orbital distances and planetary masses, we found that it is unlikely that Kepler-93b has formed with a mass high enough for its orbit to be perturbed by stellar tides, when we assume that photoevaporation is the only process that induces mass loss from the planet.

In the context of the preparation of the PLATO mission, our study proves that for the benchmark target of a solar-like star with a visible magnitude of 10, a precision of 10% in age can be achieved with a detailed seismic modelling procedure and the use of mean density inversions. We showed that this threshold of 10% is reached if a precision of about 3% in mass and 1% in radius is achieved. However, the variations of 4% in age observed when using the OPLIB opacities still advocate for caution regarding the actual accuracy of the stellar models. In this respect, further tests for benchmark stars are required to test the impact of metallicity, especially for cases deviating more significantly from the solar metallicity. Our study also underlines the relevance of inversion techniques for the PLATO mission. The inclusion of the mean density in the constraints can improve the precision of the stellar mass and radius. Inversions are feasible as long as individual acoustic oscillations are determined for a given target. This is expected to be the case for the majority of the PLATO sample of main-sequence solar-type stars ($\sim$10 000 stars). For red giants and subgiants, mixed modes can exhibit intrinsic non-linearities, but mean density inversions have been shown to be feasible for these targets using radial modes alone (Buldgen et al. 2019c). Hence, inversions are hoped to be of a great help for most of the PLATO sample.

References

Adelberger, E. G., García, A., Robertson, R. G. H., et al. 2011, Rev. Mod. Phys., 83, 195

Appourchaux, T., Antia, H. M., Ball, W., et al. 2015, A&A, 582, A25

Asplund, M., Grevesse, N., Sauval, A. J., & Scott, P. 2009, ARA&A, 47, 481

Backus, G., & Gilbert, F. 1968, Geophys. J., 16, 169

Backus, G., & Gilbert, F. 1970, Phil. Trans. R. Soc. London Ser. A, 266, 123

Baglin, A., Auvergne, M., Barge, P., et al. 2009, in Transiting Planets, eds. F. Pont, D. Sasselov, & M. J. Holman, IAU Symp., 253, 71

Bailer-Jones, C. A. L., Rybizki, J., Fouesneau, M., Mantelet, G., & Andrae, R. 2018, AJ, 156, 58

Ball, W. H., & Gizon, L. 2014, A&A, 568, A123

Ballard, S., Chaplin, W. J., Charbonneau, D., et al. 2014, ApJ, 790, 12

Barclay, T., Pepper, J., & Quintana, E. V. 2018, ApJS, 239, 2

Basu, S., & Antia, H. M. 2008, Phys. Rep., 457, 217

Bellinger, E. P., Angelou, G. C., Hekker, S., et al. 2016, ApJ, 830, 31

Bellinger, E. P., Hekker, S., Angelou, G. C., Stokholm, A., & Basu, S. 2019, A&A, 622, A130

Benomar, O., Takata, M., Shibahashi, H., Ceillier, T., & García, R. A. 2015, MNRAS, 452, 2654

Bordé, P., Rouan, D., & Léger, A. 2003, A&A, 405, 1137

Borucki, W. J., Koch, D., Basri, G., et al. 2010, Science, 327, 977

Borucki, W. J., Koch, D. G., Basri, G., et al. 2011, ApJ, 736, 19

Brown, T. M., Christensen-Dalsgaard, J., Dziembowski, W. A., et al. 1989, ApJ, 343, 526

Buldgen, G., Reese, D. R., Dupret, M. A., & Samadi, R. 2015a, A&A, 574, A42

Buldgen, G., Reese, D. R., & Dupret, M. A. 2015b, A&A, 583, A62

Buldgen, G., Reese, D. R., & Dupret, M. A. 2016a, A&A, 585, A109

Buldgen, G., Salmon, S. J. A. J., Reese, D. R., & Dupret, M. A. 2016b, A&A, 596, A73

Buldgen, G., Salmon, S. J. A. J., Godart, M., et al. 2017, MNRAS, 472, L70

Buldgen, G., Reese, D. R., & Dupret, M. A. 2018, A&A, 609, A95

Buldgen, G., Farnir, M., Pezzotti, C., et al. 2019a, A&A, 630, A126

Buldgen, G., Salmon, S., & Noels, A. 2019b, Front. Astron. Space Sci., 6, 42

Buldgen, G., Rendle, B., Sonoi, T., et al. 2019c, MNRAS, 482, 2305

Campante, T. L., Santos, N. C., & Monteiro, M. J. P. F. G. 2018, Astrophysics and Space Science Proceedings (Springer International Publishing), 49

Casagrande, L., & VandenBerg, D. A. 2014, MNRAS, 444, 392

Casagrande, L., & VandenBerg, D. A. 2018, MNRAS, 475, 5023

Cassisi, S., Potekhin, A. Y., Pietrinferni, A., Catelan, M., & Salaris, M. 2007, ApJ, 661, 1094

Chandrasekhar, S. 1964, ApJ, 139, 664

Chandrasekhar, S., & Lebovitz, N. R. 1964, ApJ, 140, 1517

Christensen-Dalsgaard, J. 2021, Liv. Rev. Sol. Phys., 18, 2

Christensen-Dalsgaard, J., Kjeldsen, H., Brown, T. M., et al. 2010, ApJ, 713, L164

Clement, M. J. 1964, ApJ, 140, 1045

Colgan, J., Kilcrease, D. P., Magee, N. H., et al. 2016, ApJ, 817, 116

Couvidat, S., García, R. A., Turck-Chièze, S., et al. 2003, ApJ, 597, L77

Cox, J. P., & Giuli, R. T. 1968, Principles of Stellar Structure (New York: Gordon and Breach)

Cumming, A., Marcy, G. W., & Butler, R. P. 1999, ApJ, 526, 890

Davies, G. R., Silva Aguirre, V., Bedding, T. R., et al. 2016, MNRAS, 456, 2183

Deheuvels, S., Michel, E., Goupil, M. J., et al. 2010, A&A, 514, A31

Dorn, C., Hinkel, N. R., & Venturini, J. 2017, A&A, 597, A38

Dressing, C. D., Charbonneau, D., Dumusque, X., et al. 2015, ApJ, 800, 135

Dziembowski, W. A., Pamyatnykh, A. A., & Sienkiewicz, R. 1990, MNRAS, 244, 542

Eggenberger, P., Buldgen, G., & Salmon, S. J. A. J. 2019, A&A, 626, L1

Elsworth, Y., Howe, R., Isaak, G. R., et al. 1995, Nature, 376, 669

Erkaev, N. V., Kulikov, Y. N., Lammer, H., et al. 2007, A&A, 472, 329

Ferguson, J. W., Alexander, D. R., Allard, F., et al. 2005, ApJ, 623, 585

Foreman-Mackey, D., Hogg, D. W., Lang, D., & Goodman, J. 2013, PASP, 125, 306

Furlan, E., Ciardi, D. R., Cochran, W. D., et al. 2018, ApJ, 861, 149

Gaia Collaboration (Brown, A. G. A., et al.) 2018, A&A, 616, A1

Gelman, A., Carlin, J., Stern, H., et al. 2013, Bayesian Data Analysis, Chapman & Hall/CRC Texts in Statistical Science (CRC Press)

Ginzburg, S., Schlichting, H. E., & Sari, R. 2018, MNRAS, 476, 759

Green, G. M., Schlafly, E. F., Finkbeiner, D., et al. 2018, MNRAS, 478, 651

Grevesse, N., & Noels, A. 1993, in Origin and Evolution of the Elements, eds. N. Prantzos, E. Vangioni-Flam, & M. Casse, 15

Høg, E., Fabricius, C., Makarov, V. V., et al. 2000, A&A, 355, L27

Howe, R., Chaplin, W. J., Davies, G. R., et al. 2018, MNRAS, 480, L79

Howe, R., Chaplin, W. J., Basu, S., et al. 2020, MNRAS, 493, L49

Huber, D., Chaplin, W. J., Christensen-Dalsgaard, J., et al. 2013, ApJ, 767, 127

Iglesias, C. A., & Rogers, F. J. 1996, ApJ, 464, 943

Irwin, A. W. 2012, Astrophysics Source Code Library [record ascl:1211.002]

Jørgensen, A. C. S., Montalbán, J., Miglio, A., et al. 2020, MNRAS, 495, 4965

Kosovichev, A. G. 1988, Sov. Astron. Lett., 14, 145

Kosovichev, A. G., Schou, J., Scherrer, P. H., et al. 1997, Sol. Phys., 170, 43

Kubyshkina, D., Fossati, L., Erkaev, N. V., et al. 2018, ApJ, 866, L18

Landi, E., & Testa, P. 2015, ApJ, 800, 110

Lecavelier Des Etangs, A. 2007, A&A, 461, 1185

Lund, M. N., Miesch, M. S., & Christensen-Dalsgaard, J. 2014, ApJ, 790, 121

Lynden-Bell, D., & Ostriker, J. P. 1967, MNRAS, 136, 293

Marcy, G. W., Isaacson, H., Howard, A. W., et al. 2014, ApJS, 210, 20

Matt, S. P., Brun, A. S., Baraffe, I., Bouvier, J., & Chabrier, G. 2015, ApJ, 799, L23

Matt, S. P., Brun, A. S., Baraffe, I., Bouvier, J., & Chabrier, G. 2019, ApJ, 870, L27

Mazeh, T., Perets, H. B., McQuillan, A., & Goldstein, E. S. 2015, ApJ, 801, 3

Miglio, A., & Montalbán, J. 2005, A&A, 441, 615

Owen, J. E., & Wu, Y. 2017, ApJ, 847, 29

Paquette, C., Pelletier, C., Fontaine, G., & Michaud, G. 1986, ApJS, 61, 177

Pezzotti, C., Eggenberger, P., Buldgen, G., et al. 2021, A&A, 650, A108

Pijpers, F. P., & Thompson, M. J. 1994, A&A, 281, 231
Pitrou, C., Coc, A., Uzan, J.-P., & Vangioni, E. 2018, Phys. Rep., 754, 1
Potekhin, A. Y., Baiko, D. A., Haensel, P., & Yakovlev, D. G. 1999, A&A, 346, 345
Privitera, G., Meynet, G., Eggenberger, P., et al. 2016, A&A, 593, L15
Proffitt, C. R., & Michaud, G. 1991, ApJ, 380, 238
Rao, S., Meynet, G., Eggenberger, P., et al. 2018, A&A, 618, A18
Rauer, H., & Heras, A. M. 2018, in Space Missions for Exoplanet Science: PLATO, eds. H. J. Deeg, & J. A. Belmonte, 86
Rauer, H., Catala, C., Aerts, C., et al. 2014, Exp. Astron., 38, 249
Reese, D. R., Marques, J. P., Goupil, M. J., Thompson, M. J., & Deheuvels, S. 2012, A&A, 539, A63
Rendle, B. M., Buldgen, G., Miglio, A., et al. 2019, MNRAS, 484, 771
Ricker, G. R., Winn, J. N., Vanderspek, R., et al. 2015, J. Astron. Telesc. Instrum. Syst., 1, 014003
Roweis, S. 1996, Levenberg-Marquardt Optimization (University of Toronto)
Roxburgh, I. W. 1985, Sol. Phys., 100, 21
Roxburgh, I. W. 2002, in Stellar Structure and Habitable Planet Finding, eds. B. Battrick, F. Favata, I. W. Roxburgh, & D. Galadi, ESA SP, 485, 75
Roxburgh, I. W. 2016, A&A, 585, A63
Roxburgh, I. W. 2018, ArXiv e-prints [arXiv:1808.07556]
Roxburgh, I. W., & Vorontsov, S. V. 2002a, in Stellar Structure and Habitable Planet Finding, eds. B. Battrick, F. Favata, I. W. Roxburgh, & D. Galadi, ESA SP, 485, 337
Roxburgh, I. W., & Vorontsov, S. V. 2002b, in Stellar Structure and Habitable Planet Finding, eds. B. Battrick, F. Favata, I. W. Roxburgh, & D. Galadi, ESA SP, 485, 341
Roxburgh, I. W., & Vorontsov, S. V. 2003, A&A, 411, 215
Salmon, S. J. A. J., Van Grootel, V., Buldgen, G., Dupret, M. A., & Eggenberger, P. 2021, A&A, 646, A7
Santos, A. R. G., Campante, T. L., Chaplin, W. J., et al. 2018, ApJS, 237, 17
Sanz-Forcada, J., Micela, G., Ribas, I., et al. 2011, A&A, 532, A6
Scuflaire, R., Théado, S., Montalbán, J., et al. 2008a, Ap&SS, 316, 83
Scuflaire, R., Montalbán, J., Théado, S., et al. 2008b, Ap&SS, 316, 149
Silva Aguirre, V., Davies, G. R., Basu, S., et al. 2015, MNRAS, 452, 2127
Sonoi, T., Samadi, R., Belkacem, K., et al. 2015, A&A, 583, A112
Sullivan, P. W., Winn, J. N., Berta-Thompson, Z. K., et al. 2015, ApJ, 809, 77
Suto, Y., Kamiaka, S., & Benomar, O. 2019, AJ, 157, 172
Thomas, A. E. L., Chaplin, W. J., Basu, S., et al. 2021, MNRAS, 502, 5808
Thoul, A. A., Bahcall, J. N., & Loeb, A. 1994, ApJ, 421, 828
Tu, L., Johnstone, C. P., Güdel, M., & Lammer, H. 2015, A&A, 577, L3
Van Eylen, V., Agentoft, C., Lundkvist, M. S., et al. 2018, MNRAS, 479, 4786
Vandakurov, Y. V. 1967, AZh, 44, 786
Vernazza, J. E., Avrett, E. H., & Loeser, R. 1981, ApJS, 45, 635
White, T. R., Bedding, T. R., Gruberbauer, M., et al. 2012, ApJ, 751, L36
Wright, N. J., Drake, J. J., Mamajek, E. E., & Henry, G. W. 2011, ApJ, 743, 48
Young, P. R. 2018, ApJ, 855, 15

Appendix A: Observational data

Table A.1. Observational data of Kepler-93. The observed frequencies are from Davies et al. (2016). We corrected the mode identification by one radial order, as explained in Sect. 2.

l	n	Frequency (μHz)	68% credible (μHz)
0	14	2266.65	1.78
0	15	2412.81	0.53
0	16	2558.34	1.79
0	17	2701.90	0.19
0	18	2846.59	0.14
0	19	2992.05	0.11
0	20	3137.69	0.12
0	21	3283.18	0.09
0	22	3428.94	0.13
0	23	3575.44	0.24
0	24	3724.58	1.38
0	25	3869.64	2.52
1	14	2335.79	1.50
1	15	2481.48	0.52
1	16	2625.64	1.31
1	17	2770.65	0.18
1	18	2916.15	0.12
1	19	3061.64	0.09
1	20	3207.46	0.09
1	21	3353.43	0.12
1	22	3499.47	0.15
1	23	3645.94	0.29
1	24	3792.67	0.48
1	25	3938.49	0.53
2	17	2836.77	1.05
2	18	2982.35	0.45
2	19	3129.13	0.29
2	20	3274.20	0.48
2	21	3420.75	0.45
2	22	3568.74	1.80
2	23	3715.80	2.78
2	24	3861.66	3.85

Table A.2. Observed frequency ratios of Kepler-93. These ratios were computed using the definitions of Roxburgh & Vorontsov (2003).

| Ratio type	n	Ratio	68% credible
r_{01}	15	0.028	0.006
r_{01}	16	0.031	0.011
r_{01}	17	0.027	0.005
r_{01}	18	0.023	0.001
r_{01}	19	0.022	0.001
r_{01}	20	0.021	0.001
r_{01}	21	0.019	0.001
r_{01}	22	0.018	0.001
r_{01}	23	0.021	0.002
r_{01}	24	0.032	0.008
r_{10}	15	0.029	0.007
r_{10}	16	0.030	0.010
r_{10}	17	0.024	0.002
r_{10}	18	0.022	0.001
r_{10}	19	0.022	0.001
r_{10}	20	0.020	0.001
r_{10}	21	0.018	0.001
r_{10}	22	0.018	0.001
r_{10}	23	0.027	0.005
r_{10}	24	0.031	0.010
r_{02}	18	0.067	0.007
r_{02}	19	0.067	0.003
r_{02}	20	0.059	0.002
r_{02}	21	0.062	0.003
r_{02}	22	0.056	0.003
r_{02}	23	0.046	0.012
r_{02}	24	0.060	0.021
r_{02}	25	0.055	0.032

Appendix B: Mode identification

The ϵ_{nl} phases are defined in terms of the individual frequencies and their asymptotic formulation (Roxburgh 2016):

$$\epsilon_{nl} = \frac{\nu_{nl}}{\Delta} - n - \frac{l}{2}, \tag{B.1}$$

where ν_{nl} are the individual frequencies, Δ is some arbitrary chosen reference large separation (e.g. Eq. (22) in Reese et al. 2012), n is the radial order, and l is the spherical degree.
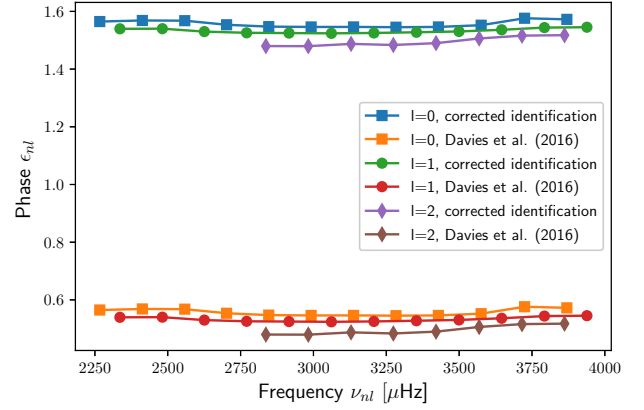
Fig. B.1. Verification of the asymptotic behaviour of the ϵ_{nl} phases. The mode identification of Davies et al. (2016) gives phases below 1, which is unexpected. The corrected identification leads to results that are comparable to Roxburgh (2016).

Appendix C: MCMC corner plot
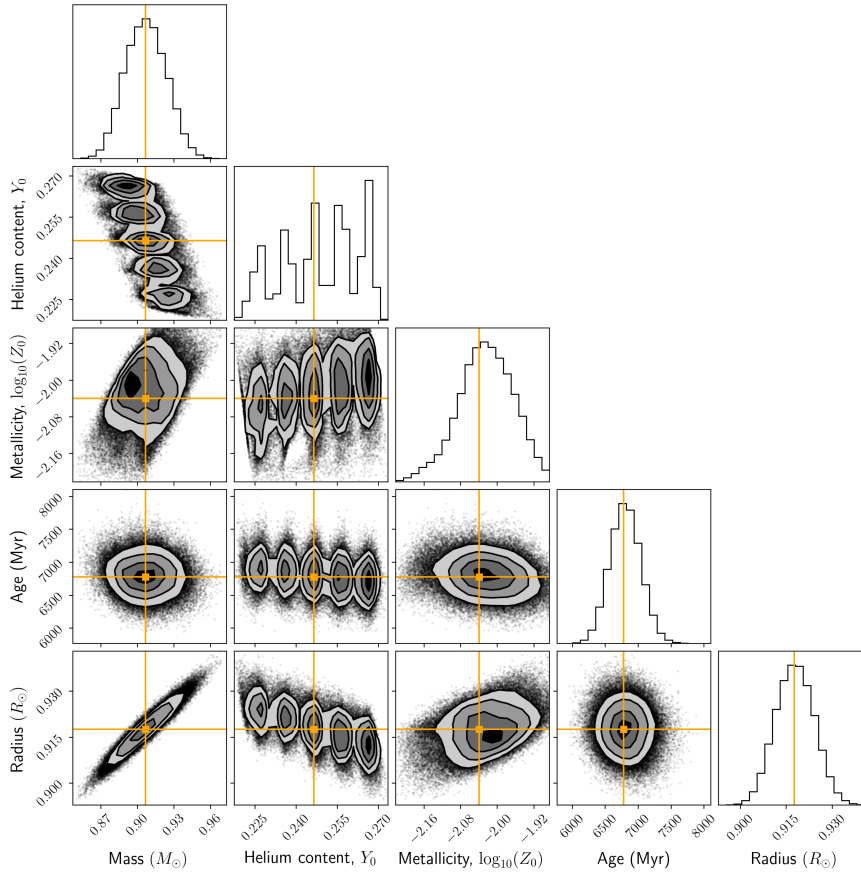
Fig. C.1. Corner plot of the MCMC fitting of the frequency ratios. The inverted mean density was part of the constraints. The optimal values are displayed in orange.